TOWARDS ACCURATE THERMAL SIMULATIONS IN PBF: A NOVEL CALIBRATION STRATEGY FOR GAUSS-GOLDAK HEAT-SOURCE MODELS

M. HOFMANN*,**, T. MAYER*

**Institute of Mechanical Systems (IMES), ZHAW Zurich University of Applied Sciences, 8401 Winterthur, Switzerland, michael.hofmann@zhaw.ch*
***Department and Institute of Materials Science (IfW), Technical University of Darmstadt, 64283 Darmstadt, Germany*

DOI 10.3217/978-3-99161-089-2-004, license CC BY 4.0

ABSTRACT

Laser Powder Bed Fusion (PBF-LB) is an advanced additive manufacturing process that fabricates near-net-shape metal components by selectively melting and solidifying powder layers with a laser beam. The intense, localized energy input generates complex thermal cycles that strongly influence microstructural evolution, residual stresses, and mechanical performance. Accurate prediction and control of this thermal history are therefore critical for optimizing part quality and process reliability.

Finite Element (FE) models employing the Gauss-Goldak heat source are widely used to simulate melt pool temperature fields and support residual stress analyses. However, the accuracy of these requires precise calibration of the heat source parameters, particularly the laser absorptivity and volumetric heat flux distribution, which vary with process conditions. This study introduces a novel calibration approach combining melt pool geometry data and in-situ thermographic measurements from the bottom side of a substrate with thermal simulations to inversely identify these parameters. The method enables tailored tuning of the thermal heat input model for specific processing conditions, substantially improving the accuracy of transient temperature predictions. Bayesian optimization was used to effectively identify absorptivity from the far-field temperature, and the shape parameters of the Gauss-Goldak heat source from the melt pool geometry.

The calibrated model demonstrates excellent agreement with experimental data, achieving deviations in simulated melt pool dimensions below 2.8%. Thereby, absorptivity emerges as the key parameter governing the far-field thermal response, underscoring the importance of its precise calibration for accurate part-scale thermal simulations. Furthermore, it is shown that, within the investigated parameter space, the shape parameters of the Goldak model exert negligible influence on the far-field temperature distribution, justifying a two-step approach. Although the calibration was performed using the Gauss-Goldak model, the approach is generalizable and can be extended to alternative heat input formulations. This enhanced modeling fidelity enabled by an accurately calibrated heat-source can facilitate more reliable residual stress and distortion forecasts in PBF manufacturing.

Keywords: powder-bed-fusion; finite element thermal analysis; model calibration; thermographic image; Bayesian optimization; stainless steel 316L, heat input model; absorptivity

INTRODUCTION

Finite Element (FE) based process simulation are widely employed to investigate the thermo-mechanical behavior of Laser Powder Bed Fusion (PBF-LB). Models exist across various length scales, with macroscale simulations targeting the prediction of temperature, residual stress, and distortion fields at layer-, and part-scale levels.

These simulations typically model the heat input by applying a volumetric heat source along the laser trajectory. A widely used heat input model in this context is the Goldak double-ellipsoid heat source, originally developed for arc-welding applications [1]. Owing to its adjustable shape parameters, the Goldak model can represent both shallow and deep melt pools, making it a flexible and widely adopted choice for PBF-LB simulations.

Most prior studies assume a constant laser absorptivity [2-6], allowing the Goldak model's shape parameters to be tuned to match experimentally observed melt pool geometries under fixed energy input conditions. However, in practice, laser absorptivity - and thus the actual energy input - is highly dependent on process parameters such as laser power, scan speed, and laser diameter [7,8]. While analytical models have been proposed to estimate absorptivity [9,10], only a few studies have directly calibrated absorptivity using temperature measurements from thermocouples [11,12] or top view thermal imaging [13], which enables the determination of the absorptivity in the order of the first decimal. However, thermocouple-based approaches are limited to single-point temperature readings and average temperatures over finite areas, thereby failing to capture spatial gradients. Furthermore, the thermal mass of the thermocouples can influence measurement accuracy, especially in thin-walled components. Top-view thermal imaging, while offering contactless measurement and high spatial resolution, suffers from uncertainty due to emissivity assumptions, which are influenced by material type, wavelength, temperature, and surface condition. Additionally, top-view imaging is often affected by dynamic process emissions such as spatter and vapor, which can obstruct the line of sight and degrade image quality.

This study introduces a novel calibration methodology under real process conditions that leverages in-situ thermal imaging from the bottom side of a thin substrate during single-track PBF experiments - a perspective not previously exploited in the literature. By imaging the process zone from below, this approach eliminates key limitations of top-view thermal imaging, such as occlusion by process emissions and uncertainty in emissivity, while preserving its advantages of high spatial resolution and non-contact measurement. Consequently, the acquired temperature field enables precise calibration of the overall heat input.

MATERIALS AND METHODS

Accurate simulation of the laser-based powder bed fusion (PBF) process requires a precisely calibrated heat input model. In particular, the model must capture the correct temperature distribution both in the near field as well as in the far field of the weld track. This necessitates an accurate estimation of the overall energy input or more specifically the effective absorptivity. Absorptivity, in the strict physical sense, is defined as the fraction of incident radiation absorbed by the material. In practice, however, the actual energy input into the process is reduced by losses due to vaporization and spatter ejection. In this study, absorptivity is defined as the net energy absorbed by the material, taking into account process related losses.

The calibration strategy for the heat input model follows two sequential steps:

I. The absorptivity is determined using in-situ thermographic measurements of a single laser track recorded from the bottom side of a thin substrate providing information on the actual energy input.
II. With determined absorptivity, the shape parameters of a Goldak double-ellipsoidal heat source model are optimized to reproduce the observed weld geometry of a single-track weld seam.

EXPERIMENTS

Single Track Experiments

Single track experiments were conducted on a conventional PBF-LB/M system (Aconity MIDI, Aconity3D, Germany). The machine is equipped with a 500 W single-mode laser (nLight, USA) featuring a Gaussian beam profile, a wavelength of 1070 nm, and a nominal focal spot diameter d_{laser} of 50 µm. By adjusting the laser focus, various spot diameters were realized.

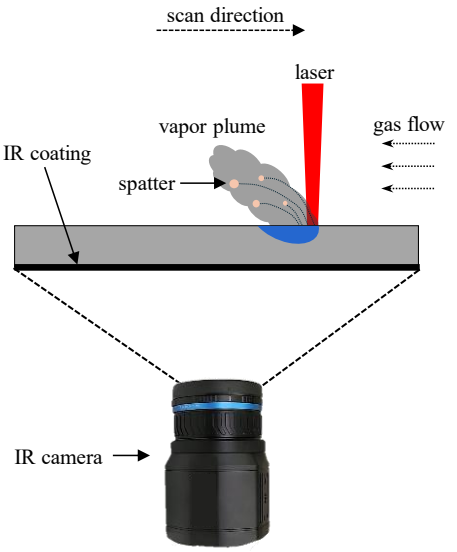

Fig. 1 Schematic illustration of the experimental setup

In each experiment, a 10 mm long laser track was scanned on a 0.5 mm thin 316L stainless steel substrate using constant laser power P_{laser} and scan speed v_{scan}. During the scanning process, the temperature field on the bottom side of the substrate was captured over time using a thermal camera, as illustrated in Fig. 1. This measurement configuration offers several advantages:

- In-situ temperature acquisition under realistic and controlled conditions
- Contactless measurement, avoiding any interference with the process
- Elimination of process emissions such as spatter or vapor on thermal imaging
- Optimal control over the emissivity of the metallic surface by applying a thermographic coating
- High spatial resolution of the recorded temperature field
- Optimal camera placement and viewing angle for thermal imaging

Thermographic measurements were conducted using a FLIR A700 (FLIR Systems, USA) uncooled microbolometer camera operating in the 7.5 µm to 14 µm spectral range with a resolution of 640x480 pixels. A macro lens was used to achieve a spatial resolution of 24 µm/pixel, sufficient to resolve the spatial thermal gradients on the bottom side of the substrate. The total field of view was approximately 15.4 mm × 11.5 mm, and the frame rate 30 Hz.

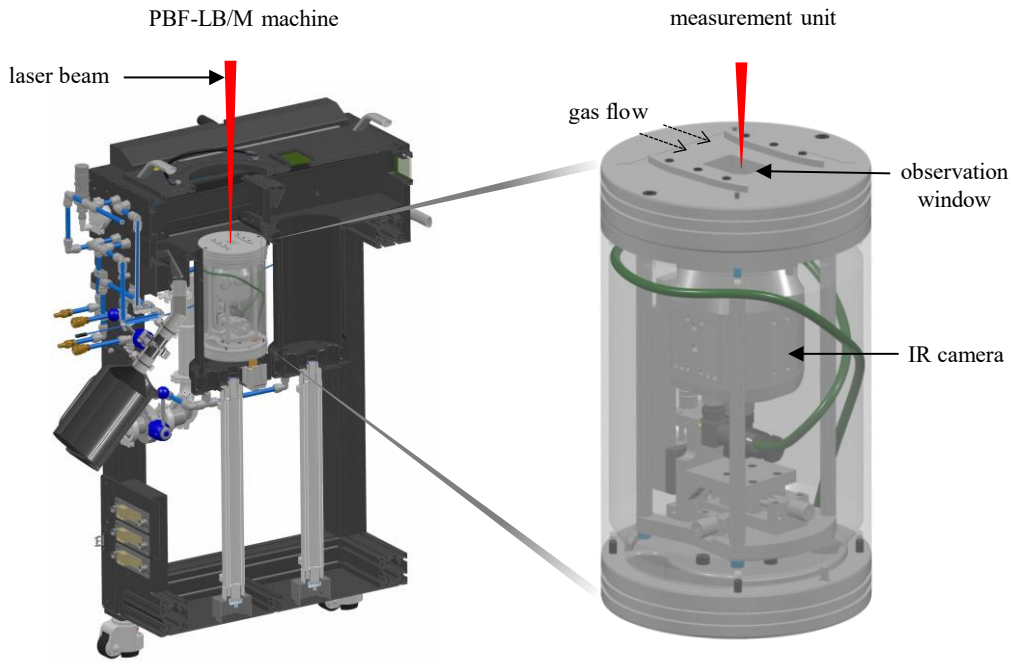

Fig. 2 Integration of the measurement unit into the PBF-LB/M machine

A custom-made measurement unit was employed to facilitate precise and reproducible camera positioning within the PBF-LB/M system. It includes a rectangular observation window on top, on which the thin substrate plate is mounted, allowing direct optical access from the camera below. The camera is placed in a vertical distance of 18 mm from the substrate bottom side. The substrate is secured using side clamps, which are screwed into the measurement unit and designed to minimize disruption of the process gas flow (see Fig. 2).

Additionally, a time synchronization between the camera and the PBF-LB/M machine was realized allowing for directly correlate the recorded thermal data with the corresponding laser position and time stamps. This is essential for the absorptivity calibration described later. Experiments were performed using three different parameter sets on bare 316L substrate plates, as listed in Table 2.

Table 1 Process parameters for the single track experiments.

Acronym	Laser Power [W]	Scan Speed [mm s^{-1}]	Laser Diameter [µm]
P150v825d50	150	825	50
P300v700d80	300	700	80
P400v550d110	400	550	110

Emissivity Calibration

Accurate thermal imaging generally requires a two-step calibration process. The first step involves calibration of the camera sensor response - involving the conversion from voltage to incident radiance. This was performed by the manufacturer using a blackbody radiator. With a known emissivity, the surface temperature can then be calculated using Planck's law. However, emissivity is not a fixed material constant; it depends on several factors, including material type, surface condition, radiation wavelength, and temperature. Therefore, a second calibration step is essential to determine the effective emissivity of the specific measurement setup, as described in the following.

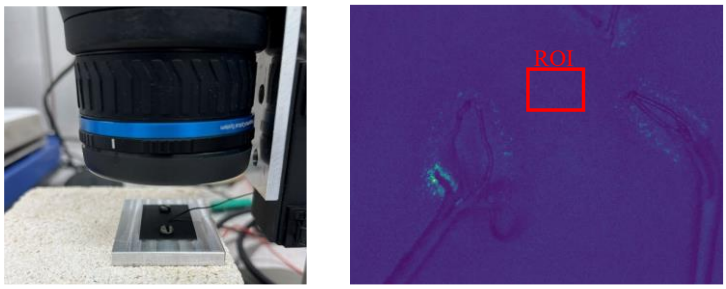

Fig. 3 Camera setup for emissivity calibration (left) and example radiometric image (right)

The emissivity calibration was carried out using the same thin substrate plate employed in the single track experiments. Type-K thermocouples were welded onto the plate using a micro-TIG welding system. Since the thermal camera observes the substrate from the bottom side, the surface was coated with a thermographic paint (LabIR Paints, Czech Republic). This coating improves the emissivity of the metallic surface, which typically exhibits low emissivity and high reflectivity. It also homogenizes the surface radiative properties, mitigating the influence of scratches or other surface irregularities. As a result, more reliable and accurate temperature measurements are achieved.

To perform the calibration, the coated substrate plate was uniformly heated and then allowed to cool in ambient air. During the cooling phase, both the thermocouple temperature readings and the radiance detected by the thermal camera were recorded. Radiance values were averaged over a region of interest (ROI) near the thermocouples but avoiding the thermocouple welds themselves, as welding can locally alter the surface properties (see Fig. 3).

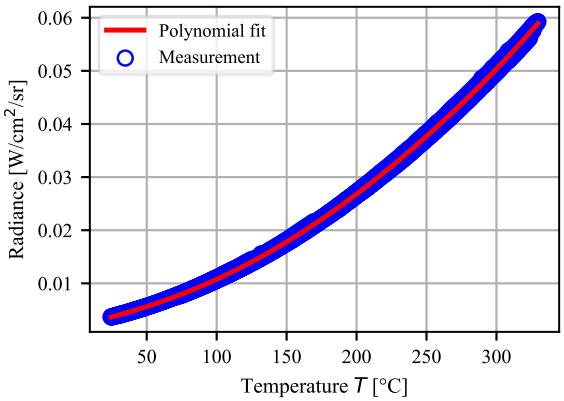

Fig. 4 Measured radiance as function of thermocouple temperature. A polynomial fit is used to generate a temperature-radiance conversion function

A total of 12 measurements were conducted resulting in a conversion plot, which correlates observed radiance to measured temperature values, as illustrated in Fig. 4. A polynomial fit was applied to the data to interpolate between recorded points. The maximum standard deviation of the fitted temperature for any measured radiance was found to be below 1.25% demonstrating high calibration accuracy. Subsequently, the radiance data recorded during the single track experiments were converted to temperature values on a pixel-wise basis using the fitted polynomial derived from the conversion plot.

SIMULATION MODEL

This section describes the FE model used for thermal calibration. The model is implemented using the commercial finite element software Abaqus 2022 (Dassault Systèmes, France). The fundamental energy balance is expressed in integral form as:

$$\int_V \rho \dot{U}\, dV + \int_S \mathbf{q_s} \cdot \mathbf{n}\, dS = \int_V q_v\, dV \tag{1}$$

where V and S are the volume and surface area of the model, respectively. ρ is the material density, $\dot{U}$ is the rate of internal energy change, $\mathbf{q_s}$ with the normal vector $\mathbf{n}$ is the surface heat flux leaving the model, and q_v is the volumetric heat input. The specific heat capacity c_p is defined as:

$$c_p(T) = \frac{\partial U}{\partial T} \tag{2}$$

Heat conduction follows Fourier's law, describing the heat flux $\mathbf{q}$ in dependence of materials conductivity k as:

$$\mathbf{q} = -k\nabla T \tag{3}$$

Applying Gauss' theorem leads to the differential form of the energy balance:

$$\rho c_p \dot{T} - \nabla \cdot (k \nabla T) = q_v \tag{4}$$

The volumetric heat input q_v is modeled using the double ellipsoidal Goldak distribution:

$$q_v = \begin{cases} \frac{6\sqrt{3} f_f \eta P_{laser}}{abc_f} \cdot \exp\left(-\frac{3x^2}{c_f^2} - \frac{3y^2}{a^2} - \frac{3z^2}{b^2}\right) & \text{if } x \geq 0 \\ \frac{6\sqrt{3} f_r \eta P_{laser}}{abc_r} \cdot \exp\left(-\frac{3x^2}{c_r^2} - \frac{3y^2}{a^2} - \frac{3z^2}{b^2}\right) & \text{if } x < 0 \end{cases} \tag{5}$$

Here x, y and z are spatial coordinates in a moving Cartesian coordinate system centered on the laser beam (Fig. 5). P_{laser} is the laser power, η is the absorptivity, and f_f and f_r are the fractions of the absorbed laser power deposited at the front and rear volume of the double ellipsoid, respectively, such that $f_f + f_r = 2$. The values are fixed at $f_f = 0.3$ and $f_r = 1.7$. The shape parameters a, b, c_f, and c_r describe the principal radii of the double ellipsoid. The relationship $a = c_f$ and $c_r = 2c_f$ is assumed [1,13], so only the parameters a and b require calibration. The volumetric heat flux distribution is implemented in the FE model using a Fortran-based DFLUX subroutine.

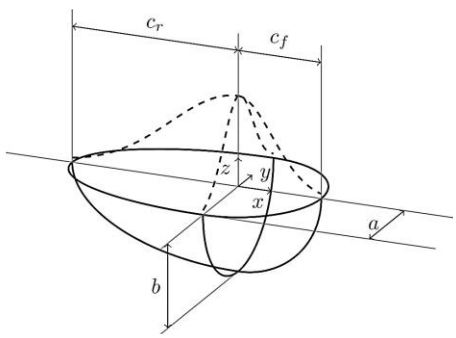

Fig. 5 Schematic illustration of the double ellipsoidal Gauss-Goldak heat flux distribution

The three-dimensional FE model represents the portion of the substrate plate within the camera's field of view. Accordingly, the model dimensions are 0.5 mm in thickness, 16 mm in length, and 6 mm in width–exploiting the symmetry of the setup. The domain is discretized using 8-node linear hexahedral elements, with a refined mesh size of 10 µm near the laser path (see Fig. 6).

The initial temperature T_{init} is set to the measured temperature of the substrate prior to laser exposure, i.e. approximately 30 °C. The lateral sides of the substrate are held at this temperature throughout the simulation.

Heat convection and radiation are considered on the top surface, while on the bottom surface only radiation is accounted for due to negligible free convection on the downward facing surface.

On the top surface, exposed to laminar process gas flow, a convective heat transfer coefficient of $h_{conv} = 80\ \mathrm{Wm^{-2}K^{-1}}$ is used, following [14]. A surface emissivity of $\epsilon = 0.4$ is applied. The symmetry plane is treated as adiabatic.

The applied boundary conditions are summarized as follows:

$$\begin{gathered} T(x,y,z,t=0) = T_{init} \quad \forall x,y,z \in V \\ T(x,y,z,t) = T_{init} \quad \forall x,y,z \in S_{side} \\ \mathbf{q_{conv}} = -h_{conv}(T - T_{init}) \quad \forall x,y,z \in S_{top} \\ \mathbf{q_{rad}} = \epsilon\sigma(T^4 - T_{init}^4) \quad \forall x,y,z \in S_{top} \cup S_{bottom} \\ \mathbf{q} = \mathbf{q_{conv}} = \mathbf{q_{rad}} = 0 \quad \forall x,y,z \in S_{sym} \end{gathered} \tag{6}$$

Here, S_{side}, S_{top}, S_{bottom} and S_{sym} denote the side, top bottom and symmetry surfaces, respectively. $\mathbf{q_{conv}}$ and $\mathbf{q_{rad}}$ are the convective and radiative heat fluxes. The Stefan-Boltzmann constant σ is set to $5.67 \times 10^{-8}\ \mathrm{Wm^{-2}K^{-4}}$.

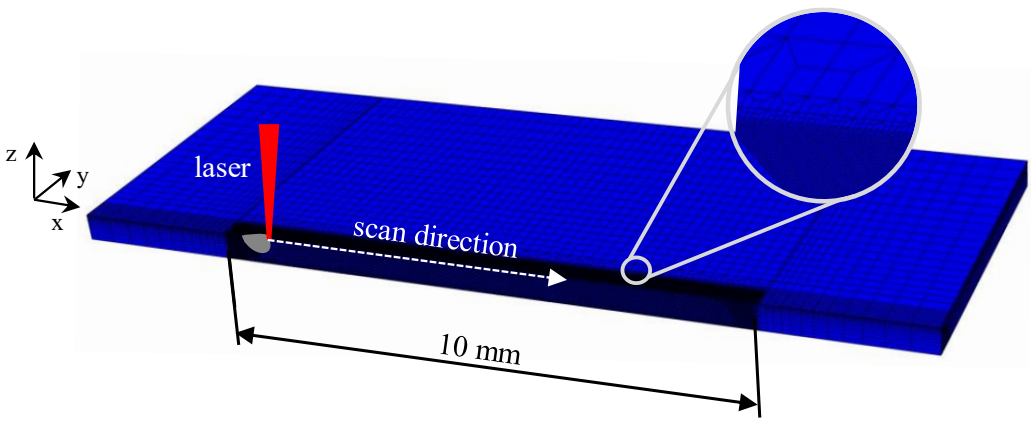

Fig. 6 Details of FE model for analysis of single track experiments

Since the volumetric heat flux q_{vol} is averaged over each time increment, the time increment size Δt_{inc} must be small enough to realistically capture the physical heating duration. During laser irradiation with constant scan speed v_{scan}, the physical exposure time corresponds to the time it takes the laser beam to traverse a point, typically estimated as the laser spot diameter d_{laser} divided by v_{scan}. For the calibration of the heat source shape parameters, a time increment size of half this exposure time is used:

$$\Delta t_{inc} = \frac{d_{laser}}{2v_{scan}} \tag{7}$$

Temperature-dependent material properties are used for the simulation, see Fig. 7. Experimental measurements were conducted to determine the density, thermal conductivity, and specific heat capacity of 316L stainless steel from room temperature up to the melting point. To extend these properties beyond the melting point, data from Choong [15] is

incorporated. Latent heat of fusion is accounted for by augmenting the specific heat between the solidus and liquidus temperatures (1419 °C and 1453 °C) by 235 kJ kg^{-1}. The thermal conductivity is artificially increased to model convective Marangoni flows in the melt pool, which are not captured directly by the simulation [16]. A thermal conductivity of 120W m^{-1} K^{-1} is assumed beyond melting temperature[1] and was implemented using the Fortran-based user subroutine USDFLD.

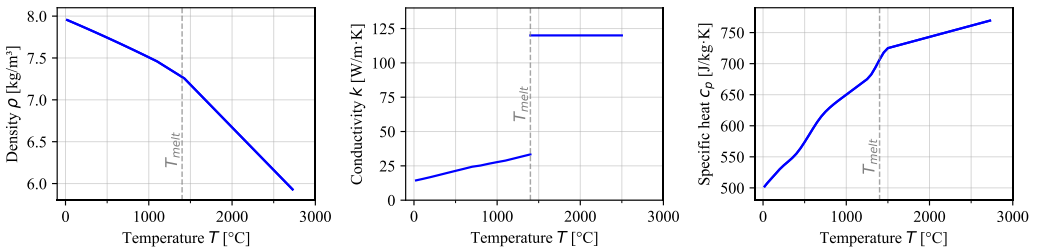

Fig. 7 Temperature dependent material properties used for the simulation

CALIBRATION

The calibration strategy of the heat input model is carried out in two sequential steps, as illustrated inFig. 8. In the first step, the absorptivity η is calibrated based on the temperature field captured by in-situ thermography. The goal is to adjust the energy input such that the simulated bottom temperature fields closely match the experimental measurements at different points in time. In the second step, the geometric shape parameters a and b of the Goldak heat source model are calibrated. This is done by comparing the simulated melt pool geometry with the experimentally observed melt pool dimensions. By adjusting the width and depth of the Goldak model, a close match to the physical melt pool is achieved.

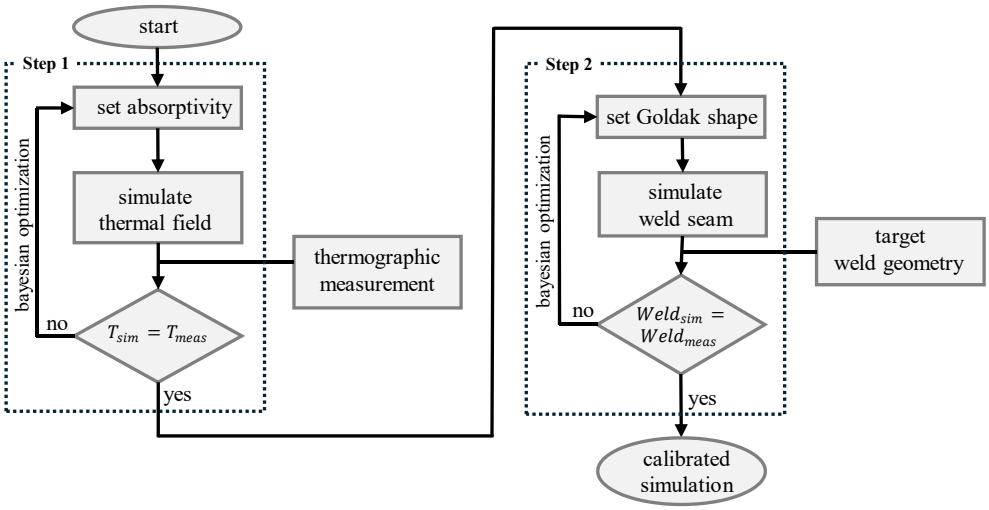

Fig. 8 Calibration strategy.

Absorptivity

To calibrate the absorptivity η, simulations are performed with fixed Goldak shape parameters ($a = 90$ µm and $b = 150$ µm). The simulated temperature field T_{sim} on the bottom side of the substrate is compared to the measured temperature field T_{meas} captured by the thermographic camera. To enable this comparison, each pixel of the thermal image was mapped both spatially and temporally to the simulation results. An algorithm was developed to determine the laser path in the coordinate system of the camera based on the thermal images. This enables the spatial mapping of the camera pixels to the simulation model's coordinate system.

As a symmetric simulation model is deployed, the measured temperature values are averaged across the left and right sides of the laser path, resulting in a symmetric averaged temperature field suitable for comparison. Rough temporal mapping is initially achieved by synchronizing the thermographic camera with the PBF-LB/M machine. However, due to high laser speeds and steep thermal gradients, this basic synchronization is insufficient. To improve accuracy, an optimized temporal alignment is determined by comparing normalized temperature fields of the simulation and measurements. This involves matching isotherms over multiple time steps to find the best temporal fit. Further details of this process are provided in the Appendix. After completing both spatial and temporal mappings, the temperature fields are compared by evaluating a loss function $\mathcal{L}_{temp}$ at $P = 3$ time points. The loss function is defined as:

$$\mathcal{L}_{temp}(\eta) = \sum_{j=1}^{P} \sum_{i=1}^{N} \frac{\left(T_{ji,meas}(x_i,y_i,t_j) - T_{ji,sim}(x_i,y_i,z=-0.5,t_j)\right)^2}{T_{ji,meas}(x_i,y_i,t_j)^2} \quad (8)$$

where N is the number of pixels used in the comparison.

Bayesian optimization[17] is subsequently employed to minimize the loss function $\mathcal{L}_{temp}$ and identify the optimal absorptivity η_{opt}. As a probabilistic, model-based optimization method, Bayesian optimization is particularly suited for expensive black-box functions, where each evaluation is time-consuming or costly. It builds a surrogate model using a Gaussian Process that approximates the true objective function and guides the search through the parameter space using an acquisition function. In this context, the objective function is $\mathcal{L}_{temp}$, quantifying the difference between measured and simulated temperature fields. The optimization proceeds iteratively by updating the surrogate model after each evaluation and selecting new candidate points that maximize the acquisition function. This allows efficient exploration of the parameter space while incorporating information from all previous evaluations. A key advantage in this application is that simulation results are reused: the loss function may be re-evaluated against different measurement datasets without rerunning simulations. This enables rapid surrogate model updates and efficient absorptivity optimization at minimal computational cost. The Matèrn 5/2 kernel is used as the covariance function, and expected improvement is employed as an acquisition function.

Shape Parameters

In the second step of the heat input model calibration, the previously calibrated absorptivity η is fixed, and the shape parameters a and b of the Goldak model are calibrated. This calibration is based on the melt pool width W and depth d, derived from a statistical model informed by multiple single track experiments [18]. Although these target values are not directly measured, they are referred to as W_{meas} and d_{meas} for consistency in notation. The simulated melt pool geometry is determined by the iso-surface corresponding to the material's melting temperature, $T_{melt} = 1424$ °C. From the simulation results, the melt pool width W_{sim} and depth d_{sim} are extracted accordingly. To quantify the difference between the simulation and the experimental targets, a loss function $\mathcal{L}_{weld}$ is defined as:

$$\mathcal{L}_{weld}(a,b) = \frac{(W_{meas}-W_{sim})^2}{W_{meas}^2} + \frac{(d_{meas}-d_{sim})^2}{d_{meas}^2} \tag{9}$$

Again, Bayesian optimization [17] is employed to minimize the loss function $\mathcal{L}_{weld}$ and identify the optimal shape parameters a and b. The Matèrn 5/2 kernel is used as the covariance function and expected improvement is used as an acquisition function.

RESULTS AND DISCUSSION

ABSORPTIVITY

The design space for the absorptivity calibration was defined in the range of 0.3 to 0.8, which corresponds to absorptivity values reported in the literature [7,8,19]. Fig. 9 (left) shows the surrogate model of the loss function $\mathcal{L}_{temp}$ for a representative measurement. The surrogate model is constructed from observation points, which are evaluations of the loss function obtained by comparing the simulated and measured temperature fields.

To identify the optimal absorptivity η_{opt} for a given measurement, the surrogate model is minimized using a differential evolution algorithm. To evaluate additional measurements of the same process parameters, existing simulation results are reused. The loss function is re-evaluated using the additional measurement data, and the surrogate model is updated accordingly. This approach enables rapid reevaluation without additional simulation effort. Fig. 9 (right) shows the surrogate models for four measurements performed under identical process conditions.

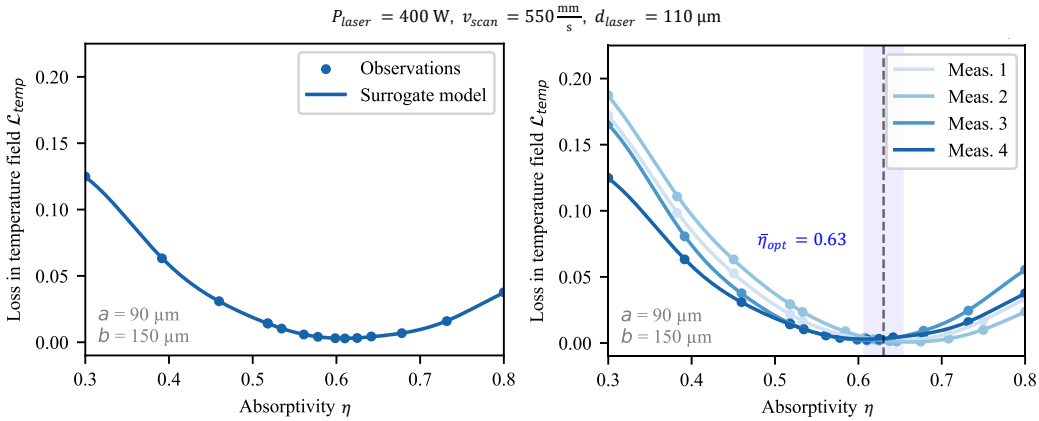

Fig. 9 Surrogate models of the loss function $\mathcal{L}_{temp}$ for the absorptivity calibration. Single measurement (left) and averaged optimal absorptivity of all measurements (right) for P400v550d110 process parameter set

Fig. 10 presents the surrogate models for two additional process parameter sets, along with their respective mean optimized absorptivity values $\bar{\eta}_{opt}$. These results are also summarized in Table 2, which includes the melt pool width W_{meas}, depth d_{meas}, and the corresponding aspect ratio $A_{meas} = d_{meas}/W_{meas}$, based on a statistical model from single track experiments. The calibrated absorptivity values fall within the expected range based on other studies [7,8]. The selected process parameters correspond to moderate to high energy densities within the stable processing window. Assuming an upper absorptivity limit of approximately

0.8 in the keyholing regime, the calibrated values appear physically reasonable. As deeper melt pools indicate a transition towards keyholing, higher absorptivity values are anticipated due to multiple reflections trapped inside the deep melt pools [20]. This trend is consistent with the results of this study: parameter sets producing higher aspect ratios also exhibit higher absorptivity values, see Table 2**.**

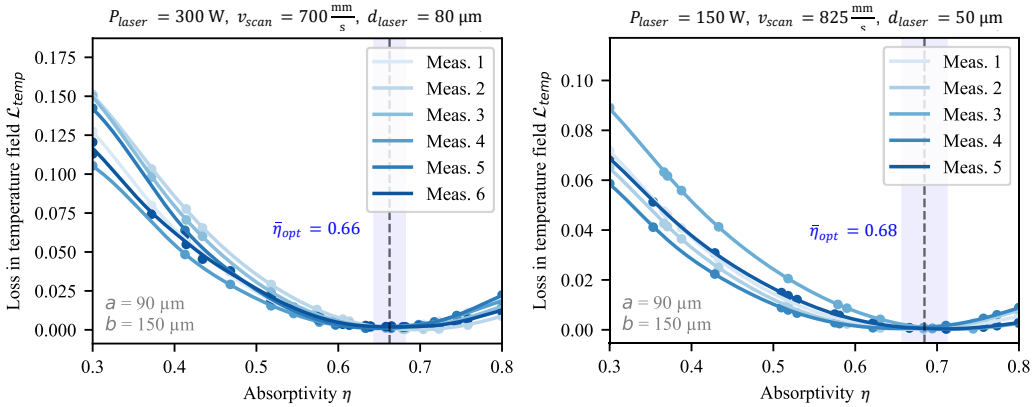

Fig. 10 Surrogate models of the loss function $\mathcal{L}_{temp}$ for the absorptivity calibration of P300v700d80 (left) and P150v825d50 (right) process parameters

Table 2 Calibrated absorptivity and weld characteristic for different process parameters.

Acronym	$\bar{\eta}_{opt}$	$\sigma_{\bar{\eta}}$	W_{meas} [µm]	d_{meas} [µm]	A_{meas}
P150v825d50	0.68	0.026	106	69	0.65
P300v700d80	0.66	0.019	170	109	0.64
P400v550d110	0.63	0.023	237	135	0.57

Fig. 11 compares the simulated and measured temperature fields for measurement 3 of the P400v550d110 process parameter set. An optimized absorptivity of 0.62 for the particular measurement was obtained from the calibration and used in the simulation. The comparison demonstrates excellent agreement between the simulated and measured temperature distributions at all three evaluated time steps.

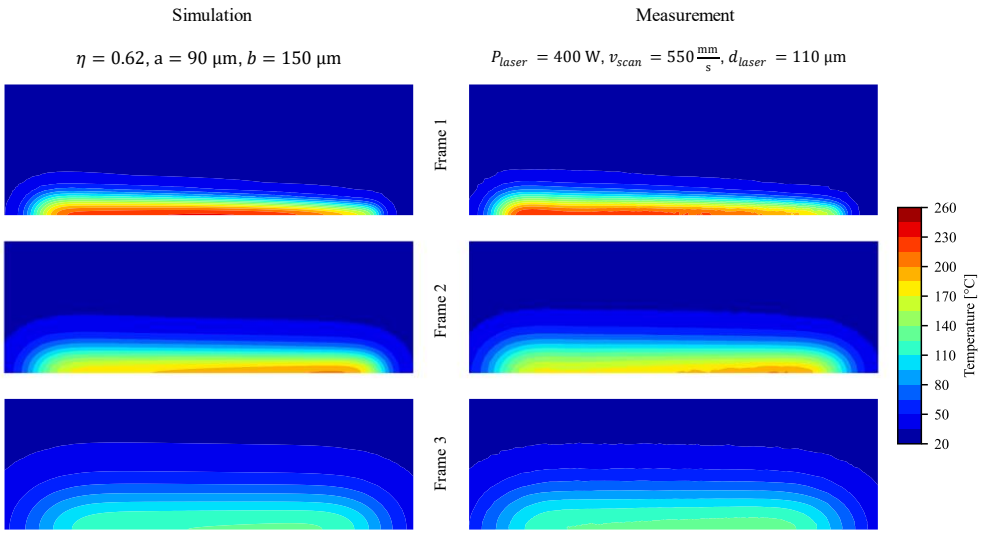

Fig. 11 Temperature field comparison of simulation and measurement 3 (optimized absorptivity of 0.62)

SHAPE PARAMETERS

Following the successful calibration of absorptivity, which leads to a good agreement with the measured temperature field in the far field, the shape parameters of the Goldak model are calibrated to better capture the thermal behavior in the near field of the weld. The loss function $\mathcal{L}_{weld}$ is minimized using Bayesian optimization. Fig. 12 illustrates an example of this optimization process. The left plot shows the surrogate model constructed from the evaluations of the loss function at various observation points, while the right plots depict the simulated weld geometry obtained using the optimized shape parameters. Table 3 summarizes the optimized Goldak shape parameters a_{opt} and b_{opt} for the three process-parameter sets. It also compares the simulated weld width W_{sim} and depth d_{sim} to the reference values W_{meas} and d_{meas}. The simulation results exhibit excellent agreement with the target geometry, with deviations for all process parameters remaining below 2.8%.

Table 3 Calibrated shape parameters and weld geometry for different process parameters.

Acronym	a_{opt} [µm]	b_{opt} [µm]	W_{sim} [µm]	W_{meas} [µm]	Dev.	d_{sim} [µm]	d_{meas} [µm]	Dev.
P150v825d50	77	121	107	106	0.7%	71	69	2.8%
P300v700d80	121	186	171	170	0.6%	109	109	0%
P400v550d110	148	199	240	238	0.8%	138	135	2.2%

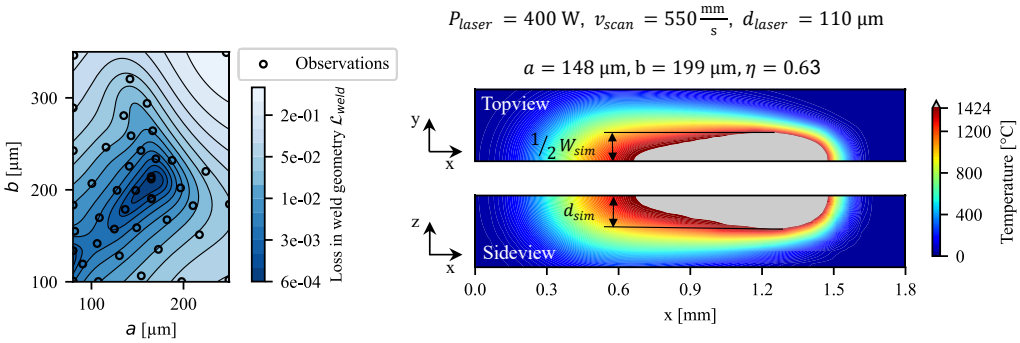

Fig. 12 Surrogate model of the loss function $\mathcal{L}_{weld}$ (left) and simulated weld geometry for optimized shape parameters a and b (right) for the process parameter set P400v550d110

VERIFICATION OF THE CALIBRATION STRATEGY

The proposed calibration strategy follows a two-step approach: first, the Goldak shape parameters are held constant to determine the absorptivity; subsequently, the absorptivity is fixed to calibrate the Goldak shape parameters. This sequential approach simplifies the optimization by reducing its dimensionality. However, it is essential to verify the validity of this strategy–specifically, whether fixing the shape parameters in the first step introduces significant variability in the determination of the absorptivity.

The strategy is valid if the shape parameters do not substantially influence the transient temperature distribution in the far field of the weld, i.e., at the bottom surface of the 0.5 mm-thick substrate plate. To verify this assumption, the first step of the calibration is repeated, but this time using the already optimized shape parameters instead of the initially fixed ones. If the recalibrated absorptivity closely matches the original value, it confirms that the two-step strategy yields reliable results. The resulting surrogate models of the loss function $\mathcal{L}_{temp}$ are shown in Fig. 13. The recalibrated averaged absorptivity values show slight deviations of 0.01 well within the standard deviation ranges observed across different measurements. These results confirm that variations in the Goldak shape parameters within the considered range do not significantly affect the far-field temperature response. Thus, the absorptivity is identified as the dominant factor for matching the far-field temperature, and the two-step calibration strategy is valid and suitable for calibrating the heat input model.

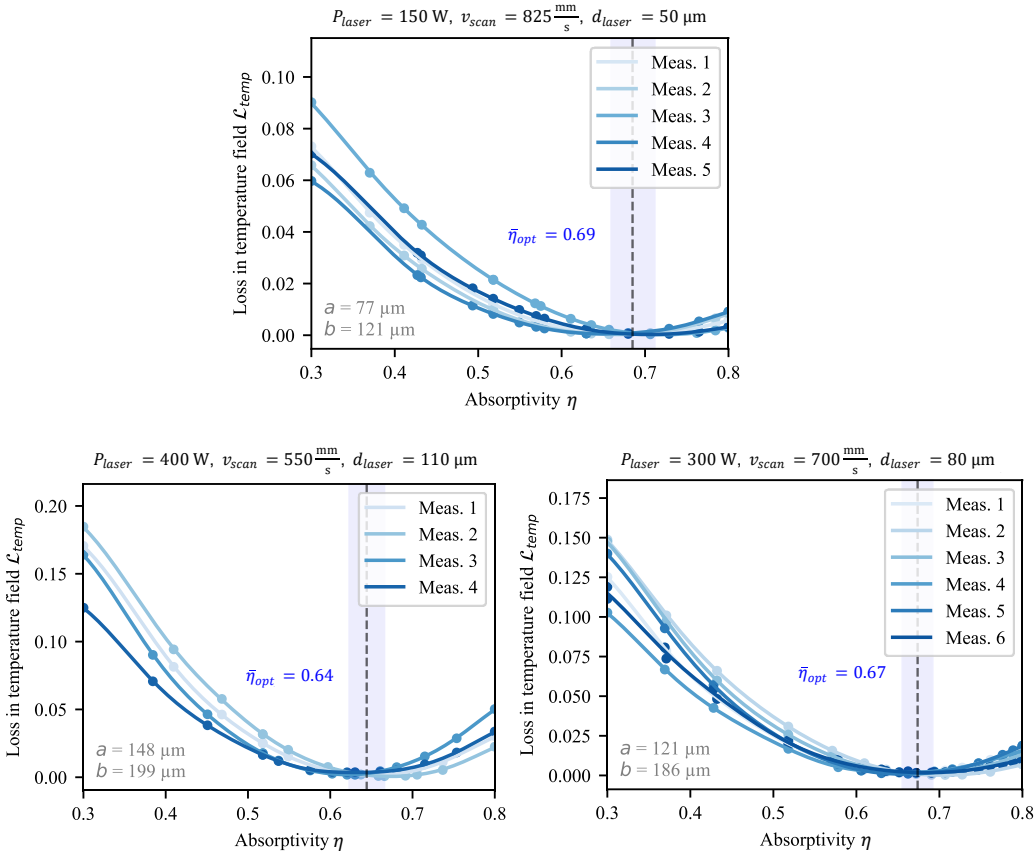

Fig. 13 Surrogate models of the loss function $\mathcal{L}_{temp}$ performed with optimized shape parameters a and b

CONCLUSIONS

This study introduces an efficient and robust two-step calibration strategy for the heat input model in PBF-LB/M simulations. High-resolution thermographic data, captured in situ from the bottom side of a thin substrate during single-track experiments, enables accurate and realistic calibration under controlled processing conditions. The laser absorptivity is calibrated using far-field temperature measurements, while the melt pool geometry serves to refine the shape parameters of a Goldak double-ellipsoid heat input model.

Bayesian optimization proves highly effective in identifying both absorptivity and shape parameters with minimal computational effort. The calibrated model demonstrates excellent agreement with experimental data, achieving deviations in simulated melt pool dimensions below 2.8%. Furthermore, it is shown that, within the investigated parameter space, the shape

parameters of the Goldak model exert negligible influence on the far-field temperature distribution. This finding validates the two-step calibration strategy, allowing for a simplified yet accurate model tuning.

Absorptivity emerges as the key parameter governing the far-field thermal response, underscoring the importance of its precise calibration for accurate part-scale thermal simulations. The proposed method demonstrates strong potential for reliable determination of absorptivity and robust thermal modeling. Although the calibration was performed using the Goldak model, the approach is generalizable and can be extended to alternative heat input formulations. Future work may apply this strategy to variable powder layer thicknesses and multi-layer builds, leveraging in situ thermal field data to further advance the understanding of heat transfer phenomena in PBF processes.

References

[1] J. GOLDAK, A. CHAKRAVARTI, M. BIBBY: 'A new finite element model for welding heat sources', *Metall Trans B*, 15 (1984), 299-305, https://doi.org/10.1007/BF02667333.

[2] E. KUNDAKCIOĞLU, I. LAZOGLU, Ö. POYRAZ, E. YASA, N. CIZICIOĞLU: 'Thermal and molten pool model in selective laser melting process of Inconel 625', *Int. J. Adv. Manuf. Technol.*, 95 (2018), 3977-3984, https://doi.org/10.1007/s00170-017-1489-1.

[3] F. AHSAN, L. LADANI: 'Temperature Profile, Bead Geometry, and Elemental Evaporation in Laser Powder Bed Fusion Additive Manufacturing Process', *JOM*, 72 (2020), 429-439, https://doi.org/10.1007/s11837-019-03872-3.

[4] S. BONTHA, N. W. KLINGBEIL, P. A. KOBRYN, H. L. FRASER: 'Effects of process variables and size-scale on solidification microstructure in beam-based fabrication of bulky 3D structures', *Materials Science and Engineering*: *A*, 513-514 (2009), 311-318, https://doi.org/10.1016/j.msea.2009.02.019.

[5] Z.-J. LI, H.-L. DAI, Y. YAO, J.-L. LIU: 'A semi-analytical model for rapid prediction of residual stress and deformation in laser powder bed fusion', *Applied Mathematical Modelling*, 125 (2024), 672-686, https://doi.org/10.1016/j.apm.2023.10.024.

[6] V. HOLLA, J. GRÜNEWALD, P. KOPP, P. M. PRAEGLA, C. MEIER, K. WUDY, S. KOLLMANNSBERGER: 'Validity of Thermal Simulation Models for Different Laser Beam Shapes in Bead-on-Plate Melting', *Integr. Mater. Manuf. Innov.*, (2024), https://doi.org/10.1007/s40192-024-00382-2.

[7] J. YE, S. A. KHAIRALLAH, A. M. RUBENCHIK, M. F. CRUMB, G. GUSS, J. BELAK, M. J. MATTHEWS: 'Energy Coupling Mechanisms and Scaling Behavior Associated with Laser Powder Bed Fusion Additive Manufacturing', *Adv. Eng. Mater.*, 21 (2019), 1900185, https://doi.org/10.1002/adem.201900185.

[8] J. TRAPP, A. M. RUBENCHIK, G. GUSS, M. J. MATTHEWS: 'In situ absorptivity measurements of metallic powders during laser powder-bed fusion additive manufacturing', *Applied Materials Today*, 9 (2017), 341-349, https://doi.org/10.1016/j.apmt.2017.08.006.

[9] T. HEELING, M. CLOOTS, K. WEGENER: 'Melt pool simulation for the evaluation of process parameters in selective laser melting', *Additive Manufacturing*, 14 (2017), 116-125, https://doi.org/10.1016/j.addma.2017.02.003.

[10] A. V. GUSAROV, I. YADROITSEV, PH. BERTRAND, I. SMUROV: 'Model of Radiation and Heat Transfer in Laser-Powder Interaction Zone at Selective Laser Melting', *Journal of Heat Transfer*, 131 (2009), 072101, https://doi.org/10.1115/1.3109245.

[11] M. CHIUMENTI, E. NEIVA, E. SALSI, M. CERVERA, S. BADIA, J. MOYA, Z. CHEN, C. LEE, C. DAVIES: 'Numerical modelling and experimental validation in Selective Laser Melting', *Additive Manufacturing*,18 (2017), 171-185, https://doi.org/10.1016/j.addma.2017.09.002.
[12] P. SCHEEL, R. WROBEL, B. RHEINGANS, T. MAYER, C. LEINENBACH, E. MAZZA, E. HOSSEINI: 'Advancing efficiency and reliability in thermal analysis of laser powder-bed fusion', *International Journal of Mechanical Sciences*, 260 (2023), 108583, https://doi.org/10.1016/j.ijmecsci.2023.108583.
[13] M. KUSANO, H. KITANO, M. WATANABE: 'Novel Calibration Strategy for Validation of Finite Element Thermal Analysis of Selective Laser Melting Process Using Bayesian Optimization', *Materials*,14 (2021), 4948, https://doi.org/10.3390/ma14174948.
[14] J. L. TAN, C. TANG, C. H. WONG: 'A Computational Study on Porosity Evolution in Parts Produced by Selective Laser Melting', *Metall. Mater. Trans. A*, 49 (2018), 3663-3673, https://doi.org/10.1007/s11661-018-4697-x.
[15] K. CHOONG: *Thermophysical Properties of Stainless Stell*, 1975.
[16] H. YIN, T. EMI: 'Marangoni flow at the gas/melt interface of steel', *Metall. Mater. Trans. B*, 34 (2003), 483-493, https://doi.org/10.1007/s11663-003-0015-z.
[17] F. NOGUEIRA: *Bayesian Optimization: Open source constrained global optimization tool for Python*, (2014), https://github.com/bayesian-optimization/BayesianOptimization (accessed January 15, 2025).
[18] M. HOFMANN, T. MAYER, F. FRISO, R. RADIS, C. KONTERMANN, M. FALK, M. OECHSNER: *Statistical modeling of melt pool geometry in PBF of 316L based on a comprehensive single-source dataset*, Unpublished Manuscript (2025).
[19] J. VOLPP: 'Laser beam absorption measurement at molten metal surfaces', *Measurement*, 209 (2023), 112524, https://doi.org/10.1016/j.measurement.2023.112524.
[20] R. FABBRO, K. CHOUF: 'Keyhole modeling during laser welding', *Journal of Applied Physics*, 87 (2000), 4075-4083, https://doi.org/10.1063/1.373033.

APPENDIX

TIME SYNCHRONISATION

For the calibration of the absorptivity by comparing simulated and measured temperature fields, it is essential to ensure that the two temperature fields are synchronized in time. A trigger signal based time synchronization between the camera and the PBF-LB/M machine was implemented, enabling the alignment of the recorded images with the corresponding laser positions and time stamps in a rough manner. However, due to high laser scan speeds and steep thermal gradient, this synchronization proved insufficiently accurate. To improve temporal alignment, the data has been post-processed.

The goal is to identify the simulation time that best matches the isothermals observed in the measurement image. This procedure involves the following steps:

I. The measured thermal field is normalized and scaled between 0 and 1. The same normalization is applied to the simulated temperature field at several time points around the pre-synchronized measurement time.

II. The normalized measurement field is compared with the normalized simulation field at these time points.
III. The simulation time point that yields the best match between simulation and measurement is selected.

Fig. 14 illustrates this procedure. The pre-synchronized measurement time is $t = 12$ ms. To refine temporal alignment, the normalized thermal fields from the simulation are analysed at various time points around $t = 12$ ms. The best match is determined by comparing the normalized simulation and the normalized measurement, i.e. Simulation at $t = 8$ ms in Fig. 14. The identified optimal time is then used for a direct comparison of the actual (non-normalized) temperature fields.

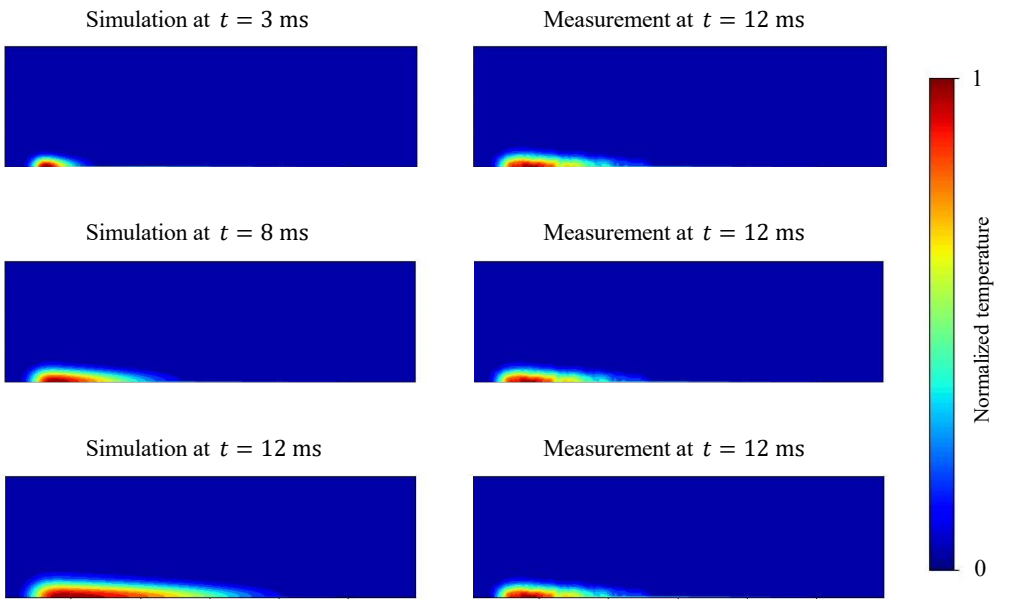

Fig. 14 Time synchronization algorithm with normalized temperature field